Resilient and Sustainable Tie-Line Bias Control for a Power System in Uncertain Environments

Iroshani Jayawardene, *Student Member, IEEE*, Ganesh Kumar Venayagamoorthy, *Fellow, IEEE*, and Xingsi Zhong

***Abstract*—Interconnected power systems with large-scale penetration of photovoltaic (PV) power introduce frequency and tie-line power flow fluctuations. This is due to the variability and uncertainty characteristics of PV power. This makes automatic generation control (AGC) to be more challenging. In other words, maintaining system frequencies and tie-line power flows at the desired values, also known as "tie-line bias control" is difficult. In this paper, an enhanced tie-line bias control method is proposed by predicting PV power generation and bus frequencies. A cyber-physical two-area power system with a large PV plant consisting of phasor measurement units (PMUs) is studied. The use of synchrophasor networks consisting of PMUs can enable smooth power system operations overcoming the challenges of PV power variability and uncertainty. However, the use of PMUs in power system control creates vulnerabilities for cyber-attacks that could jeopardize the power system operations. It is shown that the frequency prediction using a virtual synchrophasor network (VSN) can mitigate the impact(s) of denial of service (DoS) attacks on physical PMUs. Enhanced AGC performance is investigated under different weather and load conditions including a weather profile during the "Great American Eclipse" of August 21^{st}, 2017. Typical results indicate that the enhanced AGC structure provides a resilient and sustainable tie-line bias control in uncertain environments.**

***Index Terms*—cyber-physical systems, cellular computational network, echo state network, frequency predictions, PV power predictions, resilient systems, PMUs, tie-line bias control, virtual synchrophasor network.**

I. Introduction

ACCORDING to the solar energy industries association (SEIA), United States have installed 3.6 GW of solar PV capacity in Q1 2020, reaching more than 81 GW of total installed capacity, capable of powering up to 15.7 million homes [1]. During the last decade, solar power has experienced annual average growth rate of 49%. The use of solar energy is increasing worldwide due to the strong policies, rapidly declining costs, and increasing demand across the private and public sector for clean electricity. However, increasing penetration levels of solar energy introduces challenges in power system control and operation. Solar photovoltaic (PV) power has variable and uncertain characteristics, which introduce obstacles in maintaining resiliency of the power system. When the power system consists of interconnected areas, the maintenance of frequency regulations and tie-line power flow deviations is important for the resiliency of the system. The process of preserving area frequencies and tie-line power flows under desired system values (tie-line bias control) is performed by automatic generation control (AGC) [2]. AGC has become challenging with the integration of solar PV power into the power system [3].

It is important to have advanced control techniques to overcome the challenges in variable renewable energy (VRE) sources. Many studies have demonstrated the value of different strategies to improve the AGC performance in the presence of VRE sources [4]. Recent studies include an optimal mileage based dispatch (OMD) algorithm [5], a lazy reinforcement learning method [6], a predictive optimal PID plus second order derivative method [7] and, a coordinated active power control strategy [8]. The use of synchrophsor networks consisting of phasor measurement units (PMUs), can improve AGC performance to mitigate the challenges of integrating VRE. Improved AGC strategies are introduced by utilizing PMU measurements and sensor data [9]–[11]. In this paper, the importance of PV power and frequency predictions for improved tie-line bias control is explored. Predictions are obtained by exploiting PMU data of the power system synchrophasor network.

Synchrophasor networks need to be secure to ensure reliability in smart grid operation and control. Delayed or missing measurements from PMUs in real-time power system applications lead to power system frequency instability. Although, the use of virtual private networks (VPNs) eliminate many security vulnerabilities, VPNs are still vulnerable to denial of service (DoS) attacks that exploits side-channels [10].

Accurate predictions of system dynamics can overcome the challenges presented by PV power integration. Computational intelligence (CI) paradigms can address the computational challenges of PV power integration. CI paradigms are bio-inspired,

Manuscript received January 10, 2020; revised July 14, 2020 and September 23, 2020; accepted November 25, 2020. This work was supported in part by US National Science Foundation (NSF) under Grants 1312260 and 1738902 and in part by the Duke Energy Distinguished Professorship Endowment. Any opinions, findings and conclusions or recommendations expressed in this material are those of the author(s) and do not necessarily reflect the views of National Science Foundation and Duke Energy. *(Corresponding author: Iroshani Jayawardene.)*

Iroshani Jayawardene is with the Real-Time Power and Intelligent Systems Laboratory, Clemson University, Clemson, SC 29634 USA (e-mail: rjayawa@ieee.org).

Ganesh Kumar Venayagamoorthy is with the Real-Time Power and Intelligent Systems Laboratory, Clemson University, Clemson, SC 29634 USA and also with School of Engineering, University of Kwazulu-Natal, Durban 4041, South Africa (e-mail: gkumar@ieee.org).

Xingsi Zhong is with Palo Alto Networks Inc., Sunnyvale, CA USA (e-mail: zhongxingsi@gmail.com).

Digital Object Identifier 10.1109/TETCI.2020.3042812

interdisciplinary computational methods and include artificial neural networks (ANNs), fuzzy logic, evolutionary computation and swarm intelligence. CI based methods have been widely applied in smart grid applications in handling VRE sources integrated environments [12], [13].

Very short-term PV power prediction, in the order of seconds to minutes, is a challenging task under dynamic and uncertain weather conditions. PV power prediction is a big data analytics problem and has been predicted using statistical and numerical techniques [14], [15] and ANNs including echo state networks (ESNs) [13], [16]. Similarly, numerous prediction techniques have been used for power system frequency prediction. Neural network based cellular computational networks (CCNs), state space model [17], support vector regression [18] and total least squares method [19] are different methods used in predicting power system frequency. ANN has been widely used in predictions, which is capable of learning from past occurrences.

ESN is a single hidden layer recurrent neural network (RNN), which consists of a rich dynamic reservoir to make the RNN learning process faster [20]. Conventional RNN learning algorithms adapt all the weights (input, hidden, backward and output). Therefore, these learning algorithms are slow, cumbersome, and convergence cannot be guaranteed. In contrast, ESN learning process is fast, easy to implement, has the adaptive learning ability and provides better results for non-linear systems. A comparison of ESN and improved versions with several versions of RNNs is given in [21]. ESNs show lowest computation time and better accuracy compared to RNNs.

CCN is a distributed and scalable computational framework for large dynamic systems [22]. CCN consists of interconnected cells, each of which represents an individual component or a measurement unit in the system. A cell consists of a computational unit, a learning unit and a communication unit [23]. The computational unit produces an output based on the information available to the cell. The learning unit allows a cell to learn by experience in which the computational units performance is improved with time. The learning can be attained through supervised, unsupervised or reinforcement methods. The communication unit interacts with the neighboring/interconnected cells and utilizes that information in the computational process. This allows each cell to be updated about the neighboring components and use the information to adjust its own output. Communication unit and component measurements provide dynamic input-output data into a cell. Using ESN as the computational unit of CCN results in a cellular computational echo state network (CCESN). CCESN combines the advantages of both CCN and ESN, which provides a resilient and sustainable computational framework to handle the changing dynamics in power system operation.

The main contributions of this paper are:

- A virtual synchrophasor network (VSN) based on a cellular computational echo state network has been developed and implemented. The VSN provides resiliency to the physical synchrophasor network.
- Very short term photovoltaic power prediction using an echo state network has been developed and implemented.
- With PV power predictions and VSN included in AGC operations, a resilient and sustainable tie-line bias control is achievable under uncertain environments, including changing weather and load conditions.
- The VSN based on CCESN can mitigate the impact(s) of denial of service attacks on the physical synchrophasor network.

The cyber-physical power system studied in this paper consists of four layers namely; power system, AGC, prediction models, and cyber-security as shown in Fig. 1. The remainder of this paper is organized as follows; The power system and AGC layers are described in Section II. The prediction models layer is described in Section III. Descriptions of cyber-security layer, resiliency metrics, typical results and discussions are presented in Section IV. Finally, conclusions are given in Section V.

II. Cyber-Physical Power System

A diagram of the cyber-physical power system studied for resilient and sustainable tie-line bias control is given in Fig. 1. The system consists of four layers, power system (two-area four machine power system and synchrophasor network), AGC (Area-1 AGC and Area-2 AGC), prediction models (PV power predictor and VSN frequency predictor) and cyber-security (DoS attack countermeasures). Detailed descriptions of power system, synchrophasor network, AGCs and tie-line bias control are given in following subsections.

A. Two-Area Four-Machine Power System

The power system consists of two areas connected by two parallel transmission lines, each area has two synchronous generators, all rated at 900 MVA (Fig. 1). Generators G1 and G2 are in Area-1 and G3 and G4 are in Area-2. All of the generators in Fig. 1 are equipped with their primary controllers, including turbine governors, automatic voltage regulators and power system stabilizers (PSSs). The PSS structure used in this power system is a second order lead-lag compensator as shown in Fig. A.16. The PSS uses the generators' speed deviation signal ($\Delta\omega$) to generate a supplementary control signal (V_{pss}). The PSS parameters (T_{Wss}, T_{pss1}, T_{pss2}, T_{pss3}, T_{pss4}) are taken from [24]. The generators' ratings and the load values are given in Fig. 1.

The power system is developed and simulated on a real-time digital simulator (RTDS). The experimental setup consisting of the RTDS, weather station, synchrophasor network, and prediction models is given in Fig. A.17.

B. PV Power Plant

A large PV plant of capacity 210 MW is installed at Bus 12, a 230 kV utility transmission grid bus in Area-2 of the power system [25]. Real-time weather profiles, solar irradiance ($Irr(t)$) and temperature ($Temp(t)$) are used to emulate the PV plant generation. The weather profiles are monitored at the Real-Time power and Intelligent Systems (RTPIS) laboratory,

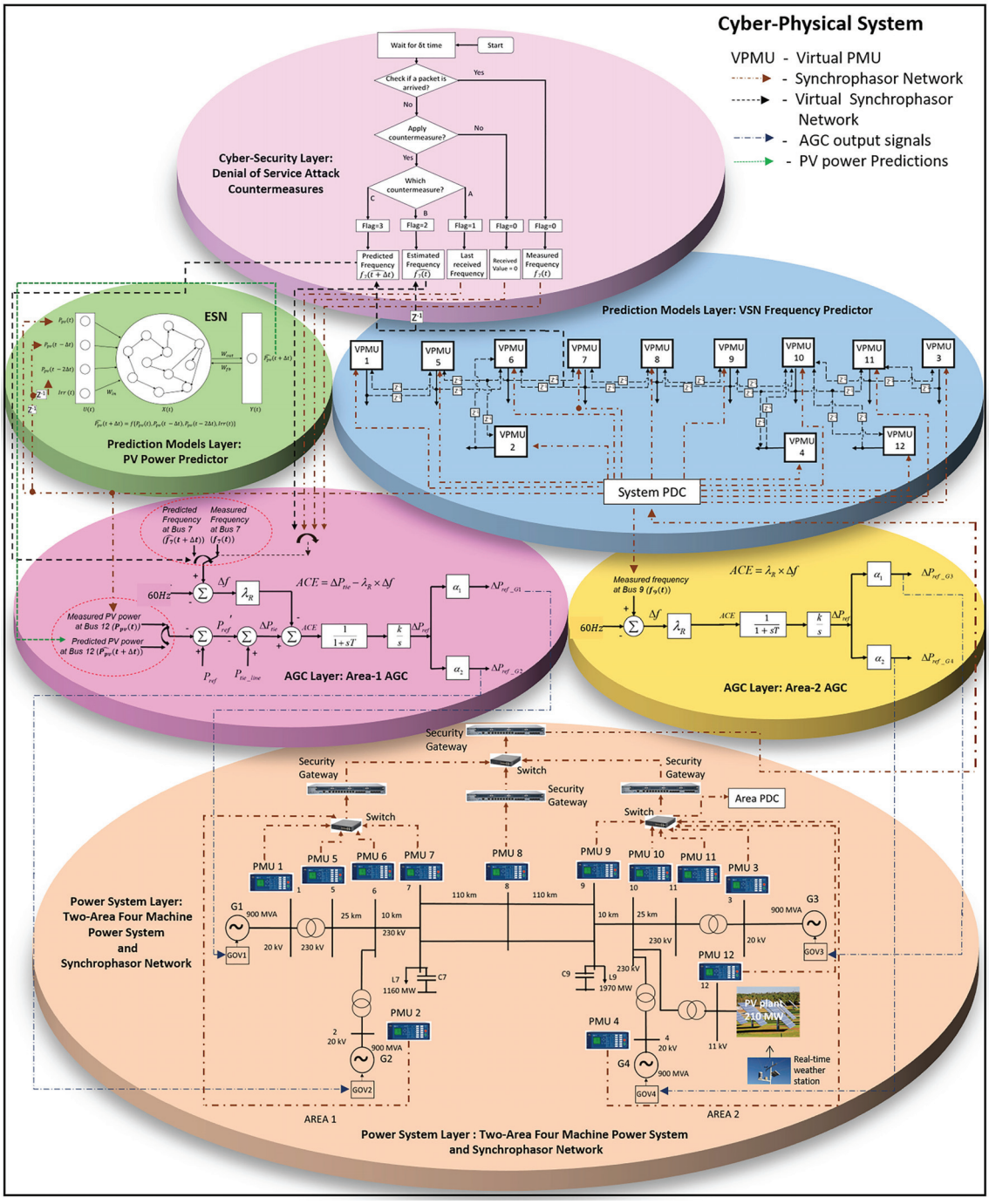

Fig. 1. Cyber-physical system consisting of the power system, AGCs, prediction models, and cyber-security layers.

Clemson University, SC, USA. Real-time weather profiles are integrated with RTDS to simulate the PV power plant.

C. Synchrophasor Network

Analogue voltages and current values are transmitted from the RTDS simulation to physical PMUs. Physical PMUs are placed at each bus of the system to to measure the bus frequencies, generator power outputs, tie-line power flow and PV plant power generation. A dedicated communication synchrophasor network is used to transmit PMU measurements to upper level layers (Fig. 1). The synchrophasor network configuration given in [10] is used for this study. The network consists of secured subnets, which are connected by a dedicated network with a security gateway protecting each secured subnet. The use of security gateways reduce the risk and cost of transmitting critical information securely through a long distance network, eliminating many vulnerabilities such as packet sniffing, data spoofing, malicious code injection, and replay attacks. VPN tunnels are established between each of the security gateways. The traffic transmitted through VPN tunnels is encrypted by the security gateway. This configuration with security gateways

eliminate many vulnerabilities but still vulnerable to DoS attacks that exploits side-channel vulnerability. Phasor data concentrator (PDC) produces time-aligned output data streams by time-synchronizing phasor data receive from multiple PMUs. There are two PDCs, each located at a secured subnet. The PMUs located at Area-1 are sending measurement to a system PDC and the PMUs located at Area-2 are sending measurement to Area PDC. The system PDC also collects measurements from Area PDC. OpenPDC is an open source synchrophasor data concentrator software, which is used as the PDC in this study.

D. Automatic Generation Control and Tie-Line Bias Control

AGC is an important control process in interconnected power system operation, which constantly operates to balance the system generation and loads and losses at a minimum cost [3]. AGC is responsible for maintaining frequency regulations and power interchange, also known as tie-line bias control.

The block diagram for the AGCs in Area-1 and Area-2 (AGC-1 and AGC-2) are given in Fig. 1. AGCs are designed with proportional-integral (PI) controllers. Corresponding AGC parameters are given in Table A.7. The objective of each area's AGC is to maintain the frequency at the nominal value ($f_7$ref). In addition, the AGC-1 also changes the tie-line power flow based on the information received from the PMU at the PV plant in Area-2. The objective is to adjust the power outputs of generators G1 and G2 to make the ACE equal to zero. The PV power generation in Area-2 offsets the power outputs of G1 and G2, thus enabling maximum PV power generation utilization in supplying the load demand in Area-2. The scheduled interchange value (reference tie-line power flow ($(P')_{\text{ref}}$)) is adjusted in real-time based on the PV power generation.

ACE calculation is given in (1).

$$ACE = \Delta P_{tie} - \lambda_R \times \Delta f \tag{1}$$

where Δf is the frequency deviation corresponding to nominal frequency and ΔP_{tie} is the tie-line power flow deviation corresponding to reference power (P'_{ref}). λ_R is the balancing authority's bias factor measured in MW/0.1Hz [2].

PV power generation and corresponding tie-line power variation obtained with AGC-1 operation on the "Great American Eclipse" of August 21^{st}, 2017 is shown in Fig. 2. Under normal operating conditions (when the PV power generation is 0 MW), a 400 MW(P_{ref}) tie-line power flow from Area-1 to Area-2 is observed.

The AGC adjusts the respective generators' governor references at every one second interval. However, the sum of the response times of AGC and generator governor is greater than one second. In other words, the inputs to the AGC at time t provides consequent changes in the system at time $t + \Delta t$. The time delay ($\Delta t > 1$) is the response time (frequency bandwidth) of the AGC and governor. The tie-line power reference (P'_{ref}) of the AGC-1 changes dynamically with respect to the current PV power generation, without considering this time delay. Therefore, the deviation in tie-line power flow (P_{tie_line}) from its commanded reference value (P'_{ref}) due to the response time of AGC and governor is minimized by predicting the PV plant power output, "Predicted PV power". The prediction time step is synchronized with the optimal frequency bandwidth (response time (Δt)) of the AGC-1 and governors of generators G1 and G2. The optimal prediction time step is determined to minimize the tie-line power flow deviation, which is founded to be approximately 30s for this study [26]. This performance is further enhanced by predicting Area-1 frequency "Predicted frequency" by considering response time for frequency. The frequency prediction time step is determined to minimize the frequency deviation, which is 1s for this study. Two prediction parameters are shown in highlighted dash circles in Fig. 1. "Predicted PV power ($\hat{P}_{pv}(t + \Delta t)$)" and "Predicted Frequency ($\hat{f}_7(t + \Delta t)$)" values are applied instead of measured PV power and frequency, respectively. A detailed comparison of AGC-1 performance with and without the use of prediction models is given in Section IV.

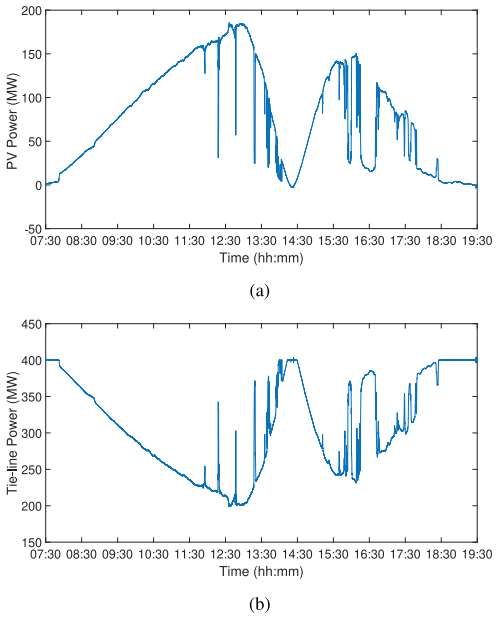

Fig. 2. During the "Great American Eclipse" of August 21^{st}, 2017. (a) PV Power generation. (b) Tie-line power flow

III. PV Power and Frequency Predictions

Real-time PMU measurements are communicated to the prediction models layer (Fig. 1) for predicting PV power and power system bus frequencies. An ESN is used as the basic prediction CI algorithm for both PV power and bus frequency predictions. The ESN and CCESN prediction models, input parameters and prediction accuracy metrics are explained in the following subsections.

A. PV Power Predictions

PV power is predicted using the ESN prediction model as shown in Fig. 1. ESN connections are initialized, so that it has a large hidden layer with coupled oscillators [20]. The hidden layer is also known as "reservoir". Input, output and hidden layer variables at time t are represented by $U(t)$, $Y(t)$ and $X(t)$ respectively. The network connections, input to hidden layer

weights (W_{in}), hidden to hidden layer weights (W) and output to hidden layer or feedback weights (W_{fb}) are randomly initialized and kept fixed throughout the process. The connections from the hidden layer (reservoir) to the output weights (W_{out}) are only learned. This makes the ESN learning process simpler and faster than conventional RNNs.

The activation for reservoir units at the $(t+1)^{th}$ time step is expressed in (2).

$$X(t+1) = f(W_{\text{in}} \times U(t) + W \times X(t) + W_{fb} \times Y(t)) \quad (2)$$

where $f(.)$ is the activation function usually chosen to be the hyperbolic tangent ($tanh(.)$) function.

Inputs to the ESN are PV power at time t ($P_{pv}(t)$), two time delayed previous PV power values ($P_{pv}(t-\Delta t)$, $P_{pv}(t-2\Delta t)$) and solar irradiance at time t ($Irr(t)$) given in (3). Predicted PV power is represented in $\hat{P}_{pv}(t+\Delta t)$.

$$U(t) = [P_{pv}(t), P_{pv}(t-\Delta t), PV(t-2\Delta t), Irr(t)] \quad (3)$$

It is important to initialize the random weights appropriately for developing an effective ESN. Hidden to hidden layer weights (W) need to be initialized, so that the activation of the reservoir state matrix ($X(t)$) remains around the same value after each iteration. This allows the input to echo around the network for a long time, which is also known as the echo state property in an ESN [20]. This is obtained by selecting an optimal spectral radius (maximum eigenvalue) for the hidden to hidden layer weights [27]. Sparse connectivity of W is important to generate large sets of loosely coupled oscillators, which allows information to reside in one part of the network without propagating to other parts of the network very quickly. Additionally, the input to hidden layer connections (W_{in}) and output to hidden layer connections (W_{fb}) must be scaled properly, which must drive the loosely coupled oscillators without erasing the information from the past. It is important to experiment different spectral radius, reservoir size and scaling parameters in obtaining optimal ESN performance.

In this study, ESN is learned using recursive least squared approach [28], which allows online model adaption. This approach is more suitable for predicting the dynamic behavior of PV power and bus frequencies in a power system.

B. Bus Frequency Predictions

An ESN based CCN, a CCESN is implemented to predict the frequencies at each bus of the system. Two-area four machine power system is modeled as a CCESN by considering each bus of the system as a cell/VPMU for the purpose of predicting the bus frequencies. CCESN based frequency predictor implemented is given in Fig. 1. Each cell of the CCESN is acting as a virtual PMU (VPMU), creating a virtual synchrophasor network. Frequency predicted at the i^{th} bus by the i^{th} cell of the CCESN is given below.

$$\hat{f}_i(t+\Delta t) = f(f_i(t), f_i(t-\Delta t), f_i(t-2\Delta t), \hat{f}_j(t)) \quad (4)$$

where $f_i(t)$ is the frequency at i^{th} cell and j is the neighboring cell number. For the power system in Fig. 1, the neighboring cells vary from 4 - 7 and the cell connectivity is topology depended.

C. Prediction Accuracy Metrics

The accuracy of the prediction models needs to be validated with standard metrics. In this study, accuracy is measured by calculating skill factor. Skill factor (SF) / forecast skill metric is used to measure PV power (SF_{PV}) and bus frequency ($SF_{\text{Frequency}}$) prediction performance as given in (5) and (6) respectively. These are defined in terms of mean square error (MSE) and are given in (7) and (8) for PV power (MSE_{PV}) and frequency ($MSE_{\text{Frequency}}$) respectively.

$$SF_{PV} = \left(1 - \frac{MSE_{PV-forecast}}{MSE_{PV-ref}}\right) \times 100\% \quad (5)$$

$$SF_{\text{Frequency}} = \left(1 - \frac{MSE_{\text{Frequency-forecast}}}{MSE_{\text{Frequency-ref}}}\right) \times 100\% \quad (6)$$

$$MSE_{PV} = \frac{1}{n}\sum_{i=1}^{n}(\hat{P}_{pv}(t) - P_{pv}(t))^2 \quad (7)$$

$$MSE_{\text{Frequency}} = \frac{1}{n}\sum_{i=1}^{n}(\hat{f}(t) - f(t))^2 \quad (8)$$

where n is the size of the data set, $MSE_{PV-forecast}$ and $MSE_{Frequency-forecast}$ are the MSEs obtained for PV and frequency prediction models and MSE_{PV-ref} and $MSE_{Frequency-ref}$ are the MSEs obtained for PV and frequency reference models. Persistence model is the simplest method of forecasting which assumes that the current value does not change at the forecast time and is used as the reference model [29]. Thus, the skill factor expresses the accuracy of the model in comparison to persistence model. Skill factor has the range $[-\infty, 100]$ where a positive SF indicates the prediction model is better than the persistence model.

Additionally, absolute percentage error (APE) and mean absolute percentage error (MAPE), given in (9) and (10), are calculated to analyze the error percentage.

$$\text{APE}_i = \left| \frac{\hat{T}(i) - T(i))}{T(i)} \right| \times 100\% \quad (9)$$

$$\text{MAPE} = \frac{1}{n}\sum_{i=1}^{n} APE_i \quad (10)$$

where $T(i)$ is the actual value and $\hat{T}(i)$ is the predicted value.

IV. Results and Discussion

A. PV Power Predictions

The optimal PV power prediction time step for the best AGC performance is found by studying different prediction time steps [26]. Best AGC performance is observed when the prediction time step (Δt) is 30 seconds. PV power predictions observed are given in Fig. 3(a). Figs. 3(b) and 3(c) are zoomed-in versions for the time periods 11:55-12:00 and 16:00-16:05, respectively. Figures indicate the accuracy of the ESN prediction model compared to persistence based reference model. According to the prediction accuracy values given in Table I, ESN prediction

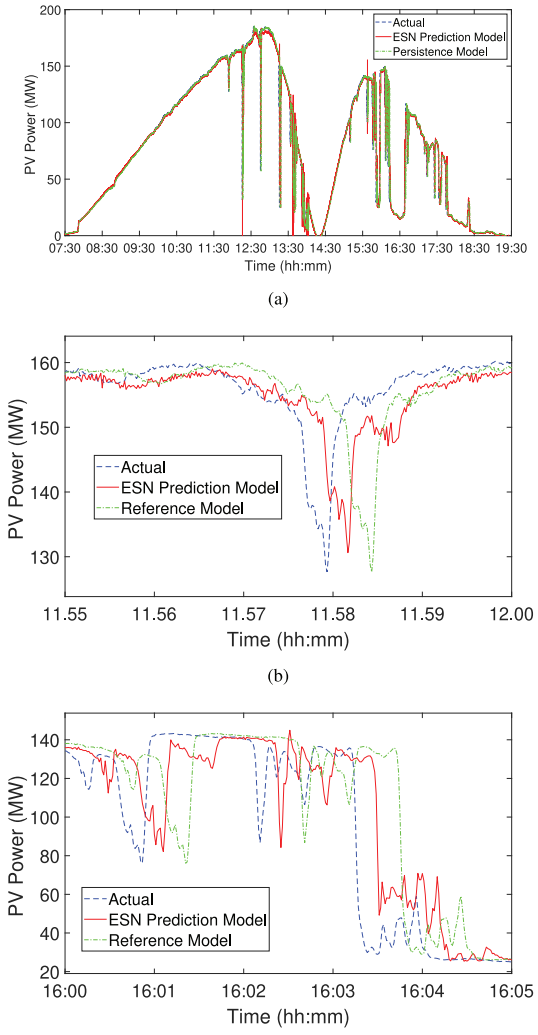

Fig. 3. (a) Actual and predicted PV power, (b) Actual and predicted PV power at 11:55-12:00, and (c) Actual and predicted PV power at 16:00-16:05.

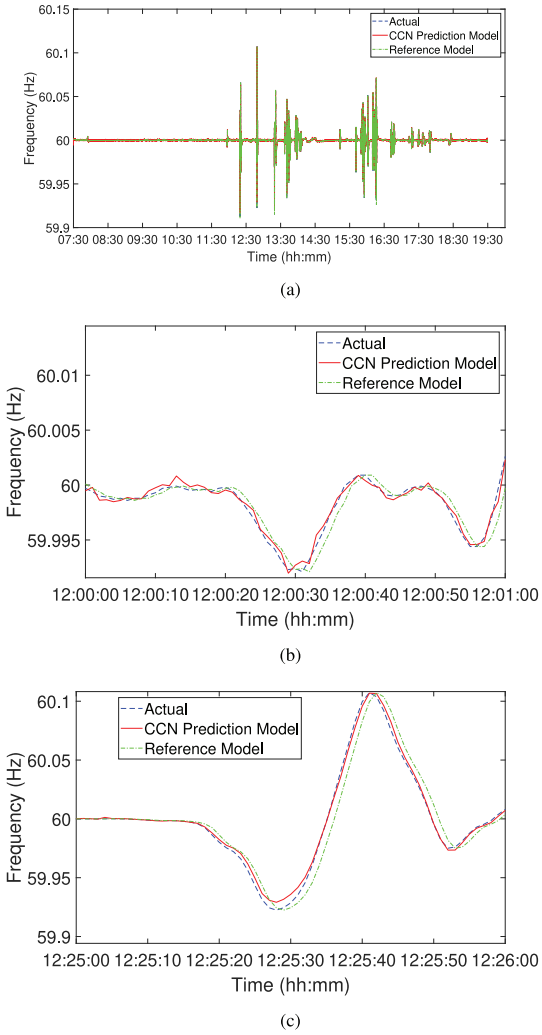

Fig. 4. (a) Actual and predicted Frequency at Bus 7, (b) Actual and predicted Frequency at Bus 7 from 12:00 to 12:01, and (c) Actual and predicted Frequency at Bus 7 from 12:25 to 12:26.

TABLE I
PV POWER AND BUS FREQUENCY PREDICTION ACCURACIES

	PV Power (Bus 12)	Frequency (Bus 7)
Prediction time step	30s	1s
Prediction model	ESN	CCESN
SF	22.08%	77.18%
MSE	0.0016 MW^2	$1.7 \times 10^{-7} Hz^2$
$MAPE$	3.19 %	3.9×10^{-4}%

model has 22% higher accuracy compared to persistence model. ESNs' MSE, MAPE values are considerably small.

B. Bus Frequency Predictions

Similar to PV power predictions, the optimal prediction time step for bus frequency predictions is identified by studying multiple time steps. The optimal prediction time step is identified as 1 second. Frequency predictions at Bus 7 observed from CCESN and reference models are given in Fig. 4(a). Figs. 4(b) and 4(c) are zoomed-in versions for the time periods 12:00 to 12:01 and 12:25 to 12:26, respectively. Fig. 4 indicates higher accuracy for the CCESN based predictions compared to the reference model. As observed in Table I, bus frequency prediction accuracy is 77% higher with CCESN compared to the reference model. CCESNs' MSE and MAPE values are considerably small.

C. Performance of AGCs and Tie-Line Bias Control

It is important to measure the resiliency in tie-line bias control using a standard performance metric. North American Electric Reliability Corporation (NERC) defines control performance standard 1 ($CPS1$) to measure the steady-state interconnection frequency in balancing authorities. Control performance standard 2 ($CPS2$) is introduced as a safety metric for $CPS1$. If $CPS1$ was the only control performance standard, the balancing authority could excessively increase or decrease the generation and obtain a very good $CPS1$, yet impact its' neighbors with

excessive power flows [2]. In this study, $CPS1$, $CPS2$ and related measures are used as the performance metrics.

Tie-line bias control performance is analyzed under four different test cases, including under real-time variable weather conditions, under severe load and weather changes, under weather conditions obtained on the "Great American Eclipse" on August 21^{st}, 2017, and under denial of service (DoS) attacks performed on physical PMUs (described in Section IV-D).

The definition for CPS1 is given in (11)–(13)

$$CPS1 = (2 - CF) \times 100\% \tag{11}$$

$$CF = \frac{(CF_{1\,\mathrm{min}})_{12\mathrm{months}}}{(\epsilon)^2} \tag{12}$$

$$CF_{1\,\mathrm{min}} = \frac{(ACE_{1\,\mathrm{min}})}{-\lambda_R} \times \Delta f_{1\,\mathrm{min}} \tag{13}$$

where $ACE_{1\,\mathrm{min}}$ is the average ACE within a minute, $\Delta f_{1\,\mathrm{min}}$ is the average Δf within a minute and $CF_{1\,\mathrm{min}}$ is the average CF within a minute and $(CF_{1\,\mathrm{min}})_{12\mathrm{months}}$ is the $CF_{1\,\mathrm{min}}$ obtained over 12 months. In this study, ϵ is considered as 18 mHz, NERC defined value for Eastern Interconnection. This is the benchmark frequency noise calculated by root mean square error of one minute averages of frequency.

If the one minute average of ACE and frequency deviation are "out of phase", then the $CPS1$ is greater than 200%. Therefore, obtaining small positive $CF_{1\,\mathrm{min}}$ or larger negative $CF_{1\,\mathrm{min}}$ indicates better performance of the system.

CPS2 related metrics are given in (14)–(16)

$$CPS2_{10\,\mathrm{min}} = \frac{\text{periods without violations}}{\text{total periods over the month}} \times 100\% \tag{14}$$

$$\text{periods without violations} = \sum \text{non-violated}_{\mathrm{ACE}} \tag{15}$$

$$\text{non-violated}_{\mathrm{ACE}} = \begin{cases} 1 & \text{, if } ACE_{10\,\mathrm{min}} < L_{10} \\ 0 & \text{, otherwise} \end{cases} \tag{16}$$

where $ACE_{10\,\mathrm{min}}$ is the average ACE within 10 minutes and L_{10} is decided based on the balancing authority size [2], in this paper $L_{10} = 30.4667$, calculated based on the Table IV in [2] assuming the balancing authority size of each Area is 1800 MW. Equation (14) is modified to consider " total periods over the simulation", instead of "total periods over the month" due to the availability of test data.

Additionally, $CPS2$ related metrics ($CPS2_{4s}$ and $CPS2_{1s}$) are calculated by considering average ACE within 4 seconds (ACE_{4s}) and 1 seconds (ACE_{1s}) for the better comparison of performance. The calculations are performed as given in (14)–(16). Total number of ACE violations observed for ACE_{4s} and ACE_{1s} are also calculated as given in (17) – (20).

$$\text{total-violated}_{\mathrm{ACE}_{4s}} = \sum \text{violated}_{\mathrm{ACE4}s} \tag{17}$$

$$\text{violated}_{\mathrm{ACE4}s} = \begin{cases} 1 & \text{, if ACE}_{4s} > L_{10} \\ 0 & \text{, otherwise} \end{cases} \tag{18}$$

$$\text{total-violated}_{\mathrm{ACE}_{1s}} = \sum \text{violated}_{\mathrm{ACE1}s} \tag{19}$$

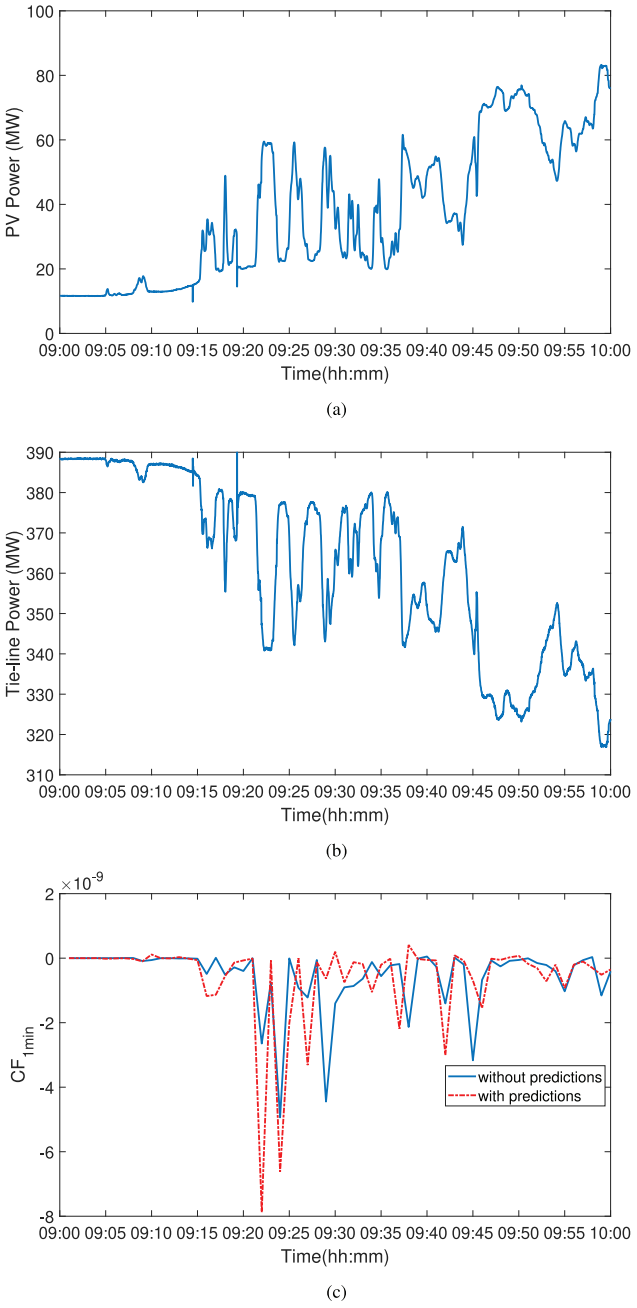

Fig. 5. (a) PV power, (b) Tie-line Power, and (c) CF_{1min} observed when PV power increases from 0 MW to 80 MW.

$$\text{violated}_{\mathrm{ACE1}s} = \begin{cases} 1 & \text{, if ACE}_{1s} > L_{10} \\ 0 & \text{, otherwise} \end{cases} \tag{20}$$

The performance of the test cases are investigated in the following subsections.

1) Real-Time Variable Weather: Tie-line bias control performance is analyzed under different weather conditions. The analysis results are categorized based on four PV power variations. PV power generation, tie-line power and $CF_{1\,\mathrm{min}}$ calculated with and without predictions obtained under four PV power variation categories are shown in Figs. 5–8. Positive and negative

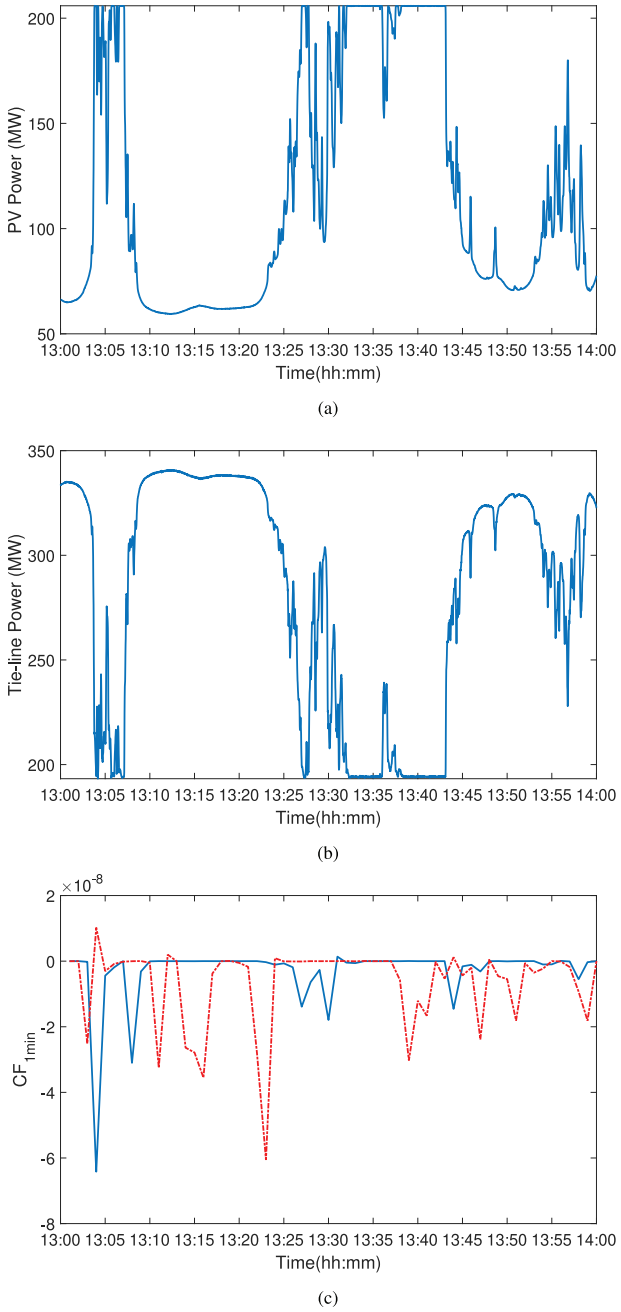

Fig. 6. (a) PV power, (b) Tie-line Power, and (c) CF_{1min} observed when PV power decreases from 200 MW to 50 MW.

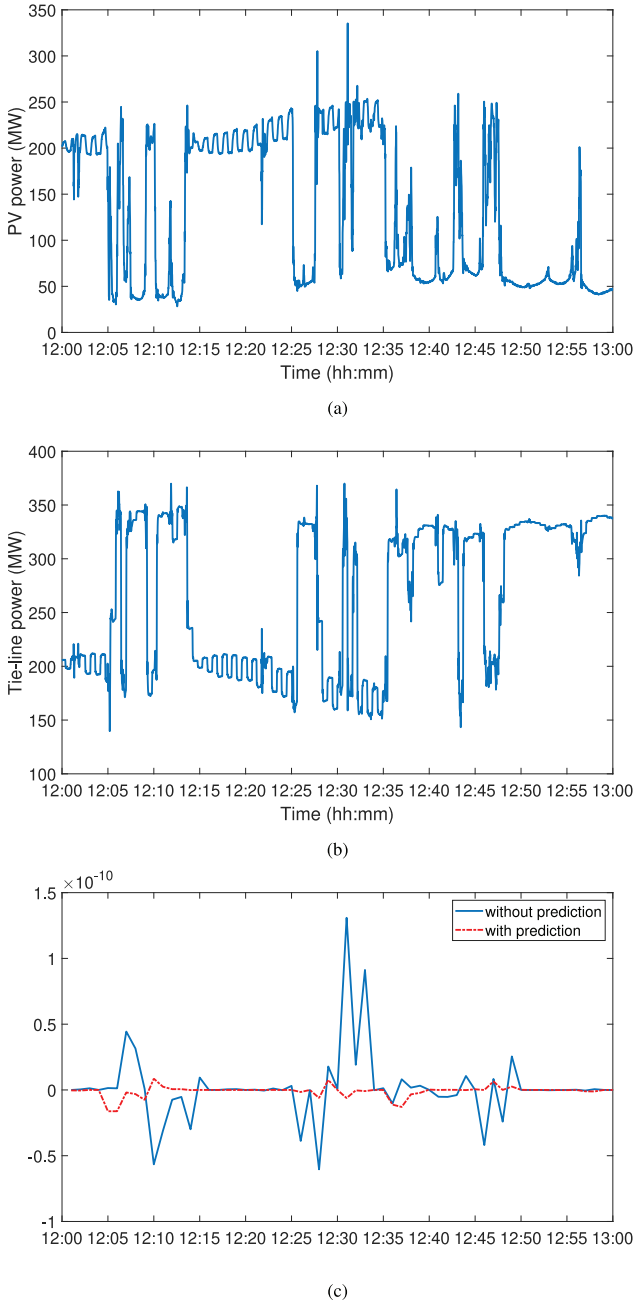

Fig. 7. (a) PV power, (b) Tie-line Power, and (c) CF_{1min} observed when PV power decreases from 200 MW to 30 MW.

$CF_{1\,\mathrm{min}}$ counts, Accumulated $CF_{1\,\mathrm{min}}$, $CPS1$, $CPS2_{10\,\mathrm{min}}$, $CPS2_{4s}$ and $CPS2_{1s}$ values calculated are recorded in Table II. All four PV power variation categories have high negative $CF_{1\,\mathrm{min}}$ counts and less positive $CF_{1\,\mathrm{min}}$ counts when predictions are applied, which indicates better performance with predictions compared to without predictions. Although, the differences between Accumulated $CF_{1\,\mathrm{min}}$ and $CPS1$ values are very small over one hour time periods analyzed in this study, long term execution of prediction algorithm increases the differences between performance metrics, indicating the usefulness of the prediction algorithm in improving AGC performance. $CPS2$ values observed for ACEs averaged within 10 minutes, 4 seconds and 1 second time periods are 100% for both test cases, indicating no under generation or over generation due to $CPS1$ improvements.

2) Load Profiles With Variable Weather: The system behavior is studied under severe weather and load changes. Simulated PV power and area load profiles are given in Fig. 9(a). Changing load profiles include loads ramping up and down in order of 10% and 20%, as shown in Fig. 9(a). The PV power is concurrently varied in maximum order of 80% with the load changes. The AGC is tested with PV power predictions (30s

TABLE II
PERFORMANCE COMPARISON UNDER VARIABLE WEATHER CONDITIONS

Metric		PV Change Level							
		0 - 80 MW		200 - 50 MW		200 - 30 MW		160-140 MW	
		Without Predictions	With Predictions	Without Predictions	With Predictions	Without Predictions	With Predictions	Without Predictions	With Predictions
CF_{1min} count	Positive	10	09	20	17	51	41	51	48
	Negative	49	50	39	42	38	48	28	31
Accumulated CF_{1min}		-3.3097×10^{-8}	-3.5712×10^{-8}	-5.0545×10^{-7}	-5.7360×10^{-7}	1.4248×10^{-10}	-6.8486×10^{-11}	7.6731×10^{-12}	2.3734×10^{-12}
$CPS1(\%)$		200.0290	200.0313	200.1556	200.3472	199.9999	200.0001	200.0000	200.0000
$CPS2_{10min}(\%)$		100	100	100	100	100	100	100	100
$CPS2_{4s}(\%)$		100	100	100	100	100	100	100	100
$CPS2_{1s}(\%)$		100	100	100	100	100	100	100	100

TABLE III
PERFORMANCE COMPARISON UNDER WEATHER AND LOAD CHANGES

Metric		Area-1 Load Change		Area-1 and Area-2 Load Change		
		Without Predictions	With Predictions ($\Delta t_{pv} = 30s$, $\Delta t_{freq} = 1s$)	Without Predictions	With Predictions ($\Delta t_{pv} = 30s$, $\Delta t_{freq} = 1s$)	With Predictions ($\Delta t_{pv} = 4s$, $\Delta t_{freq} = 1s$)
CF_{1min} count	Positive	37	27	41	31	38
	Negative	24	34	20	30	23
Accumulated CF_{1min}		0.1495×10^{-7}	-0.1678×10^{-7}	0.1261×10^{-6}	0.0972×10^{-6}	0.3070×10^{-6}
$CPS1(\%)$		199.9869	200.0147	199.8895	199.9149	199.7311
$CPS2_{10min}(\%)$		100	100	100	100	100
$CPS2_{4s}(\%)$		91	94	91	94	91
$total - violated_{ACE_{4s}}$		79	51	78	52	79
$CPS2_{1s}(\%)$		91	95	92	95	91
$total - violated_{ACE_{1s}}$		304	174	298	170	311

ahead and 4s ahead) and 1s ahead Area-1 frequency predictions. AGC performance with prediction cases are compared with that of conventional AGC including measured parameters. Obtained performance metrics including positive and negative $CF1_{min}$ counts, accumulated $CF1_{min}$, $CPS1$, $CPS2$ and total violated ACE values are given in Table III. Two main test cases are considered, Area-1 load changes with concurrently changing PV power generation and Both Area-1 and Area-2 loads change with concurrently changing PV power. Better performances are observed for AGC with 30s ahead PV power predictions and 1s ahead bus frequency predictions for both test cases. The comparison of tie-line power flow deviation, $CF1_{min}$, and Area-1 ACEs observed with and without application of predictions are given in Figs. 9(b)–9(d). However, 4s ahead PV power predictions does not show any enhanced performance, which justify the importance of selecting optimal prediction time step. Although the $CPS2_{10\,\mathrm{min}}$ is 100% for all the scenarios, $CPS2_{4s}$, $CPS2_{1s}$ and total violated ACE counts show better values for the AGC with optimal prediction time step. Higher ACE values are expected with the non-confirming load changes. Fig. 11 shows an over-frequency condition caused by load decreasing concurrently with PV power increasing (tie-line power flow is decreased). Fig. 12 shows an under-frequency condition caused by load increasing concurrently with PV power decreasing (tie-line power flow is increased). The improvements in tie-line power flow deviation, frequency deviations and ACEs observed with predictions at these scenarios as shown in Figs. 11 and 12.

TABLE IV
PERFORMANCE COMPARISON UNDER ECLIPSE DAY WEATHER CONDITIONS

Metric		Without Predictions	With Predictions
CF_{1min} count	Positive	68	61
	Negative	411	418
Accumulated CF_{1min}		-2.5030×10^{-7}	-2.8739×10^{-7}
$CPS1(\%)$		200.2391	200.2522
$CPS2_{10min}(\%)$		100	100
$CPS2_{4s}(\%)$		100	100
$CPS2_{1s}(\%)$		100	100

3) The "Great American Eclipse" of August 21^{st}, 2017*:* The system resiliency is also analyzed with weather data observed on the "Great American Eclipse" of August 21^{st}, 2017. PV power generation, tie-line power flow and calculated $CF_{1\,\mathrm{min}}$ with and without predictions are shown in Fig. 10. Positive and negative $CF1_{min}$ counts, Accumulated $CF1_{min}$, $CPS1$ and $CPS2$ values are given in Table IV. Similar results are observed as in variable weather conditions described in section 1), indicating improvements under predictions. However, long term application of prediction algorithm can guarantee higher percentage of accuracy.

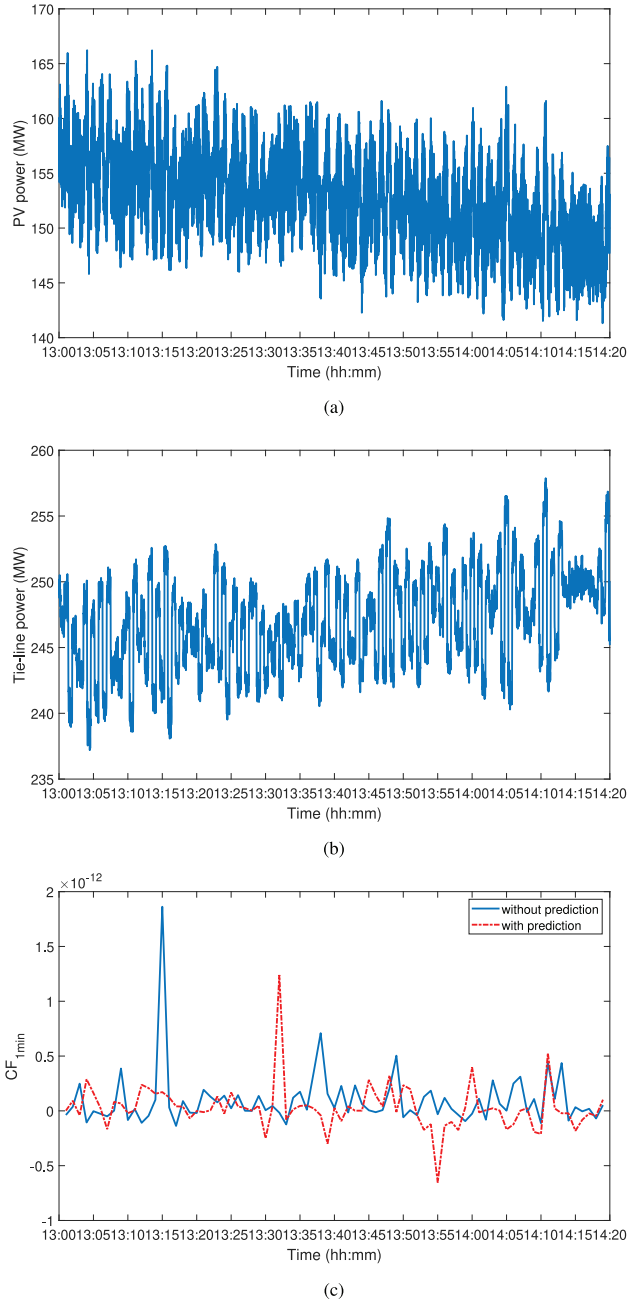

Fig. 8. (a) PV power, (b) Tie-line Power, and (c) CF_{1min} observed when PV power increases from 160 MW to 140 MW.

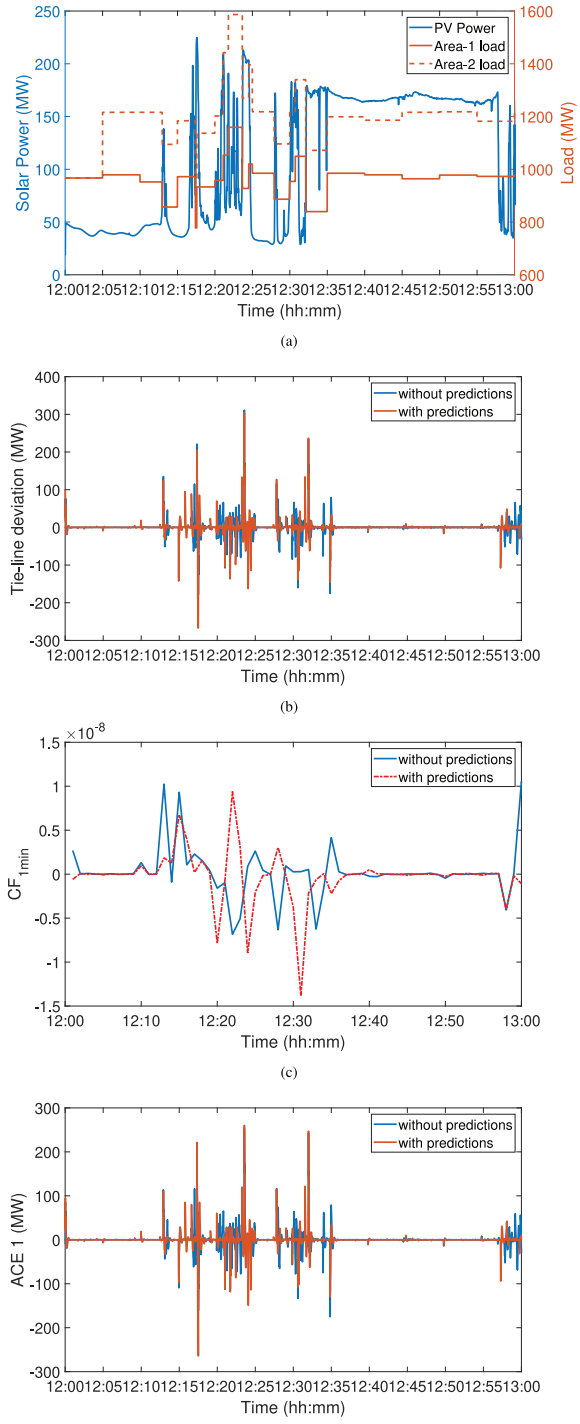

Fig. 9. (a) PV power, Area-1 load and Area-2 load profiles, (b) Tie-line Power, (c) CF_{1min}, and (d) ACE observed under load changes with variable weather.

D. Resilience to Denial of Service (DoS) Attacks

The dedicated synchrophasor network studied in this paper consists of security gateways and VPNs, eliminates many vulnerabilities but still vulnerable to denial of service (DoS) attacks. Therefore, the proposed resilient and sustainable tie-line bias control is analyzed under DoS attacks performed on the primary PMU of the system (PMU at Bus 7), on PMUs at Buses 6 and 7, and on PMUs at Buses 6, 7 and 8, where Buses 6 and 8 are the neighbors of Bus 7.

1) DoS Attack Detection: In OpenPDC, the time required to arrive all the data for a particular time frame is measured by a parameter called "Lag Time (δt)". If the measurements are expected but not received within the δt time window, the OpenPDC recognizes these measurements as missing/delayed data. These missing data positions are filled in order to keep the format of the aligned data packet fixed. A flag in the aligned data packet is set to indicate the data is invalid [30]. The missing data positions are often set to zeros. When a DoS attack is

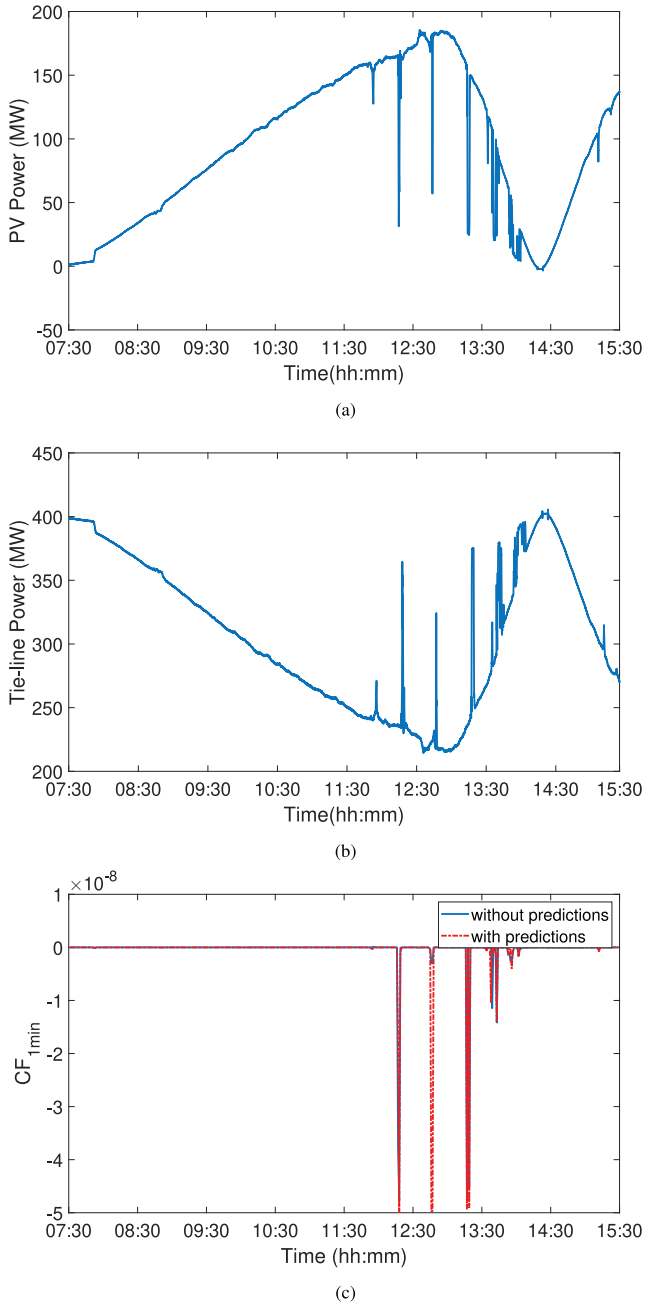

Fig. 10. (a) PV power, (b) Tie-line Power, and (c) CF_{1min} observed on the "Great American Eclipse" of August 21^{st}, 2017.

performed, that is when the attacker drops all measurement data from a PMU without interrupting the connection, PMU measurement packets are not delivered to PDC within the expected time window ("Lag Time (δt)"). The PDC set the invalid flag for the aligned data packet and send zeros instead of missing measurements.

2) Countermeasures: In this paper, PMU 7 located at Bus 7 (Fig. 1), is used to provide frequency measurement ($f_7(t)$) to the AGC in Area-1, which is the primary PMU of the system. Flow chart for the possible scenarios during a DoS attack on PMU 7 is given in Fig. 1, "Denial of Service Attack Countermeasures" layer. At each time step t, the PDC waits for δt time window until the PMU measurements are arrived. Then at $t + \delta t$, PMU packet flag status is checked to detect if there is an attack. Based on the flag status, multiple test scenarios are performed [10].

- Scenario 1: If the packet is arrived at $t + \delta t$, set the flag $=$ 0 and the measured value $f_7(t)$ is sent to AGC control
- Scenario 2: If the packet is not arrived $t + \delta t$, set the flag $= 0$ and the PDC filled data value (typically 0) is sent to AGC control
- Scenario 3: If the packet is not arrived $t + \delta t$, set the flag $= 1$ and countermeasure A (Last received valid data point) is sent to AGC control
- Scenario 4: If the packet is not arrived $t + \delta t$, set the flag $= 2$ and countermeasure B (Estimated frequency $\hat{f_7(t)}$) is sent to AGC control
- Scenario 5: If the packet is not arrived $t + \delta t$, set the flag $= 3$ and countermeasure C (CCESN based VSN predicted frequency $\hat{f_7(t + \Delta t)}$) is sent to AGC control

Scenarios for flag $= 0, 1, 2$ (normal condition, countermeasure A and countermeasure B) have been discussed in [10]. In this paper, flag $= 3$ (countermeasure C) scenario is introduced.

3) Multiple DoS Attacks: According to the topology of the power system (Fig. 1), Bus 6 and 8 are the neighboring cells of the Bus 7. CCESN based frequency prediction results observed when Bus 7 PMU is attacked, when both Bus 7 and Bus 6 PMUs are attacked, when all three PMUs (Bus 6, 7 and 8) are attacked are given in Figs. 13, 14, and 15 respectively. Prediction accuracy measures are presented in Table V. A three phase-to-ground fault is performed at Bus 8 (the tie-line power connecting Bus) while PMUs (at Bus 7, Bus 6, and Bus 8) are blocked. According to the Figs. 13–15 and Table V, VSN provides good prediction results although the neighboring cell PMUs are blocked. Frequency measurements among neighboring cells are related due to the network topology. Therefore, VSN cells can use neighboring PMU measurements to approximate missing data. However, prediction accuracies are degrading when the number of dropped PMU count is increased. However, it is still possible to use the predicted frequencies for AGC operation.

Tie-line bias control performance is analyzed under DoS attacks with the weather and load profiles given in Fig. 9(a). PMUs are blocked around 12:13, where PV power is increased from 50 MW to 150 MW and area loads are decreased by 10%. Performance metrics calculated are given in Table VI. A negative $CPS1$ value is observed for Scenario 2, indicating the system vulnerability to DoS attack. Scenarios 3 and 4 (with countermeasures A and B respectively) shows better $CPS1$ values, however the $CPS2_{4s}$ and $CPS2_{1s}$ values are low for both cases compared to scenario 5 (countermeasure C). Lower $total - violated_{ACE_{4s}}$ and $total - violated_{ACE_{1s}}$ values are observed for countermeasure C compared countermeasures A and B. Three cases under countermeasure C include when PMU 7 is attacked, when PMUs 6 and 7 are attacked, and when PMUs 6, 7, and 8 are attacked. Improved $CPS1$, $CPS2$ and total violated ACE values are illustrated with countermeasure C.

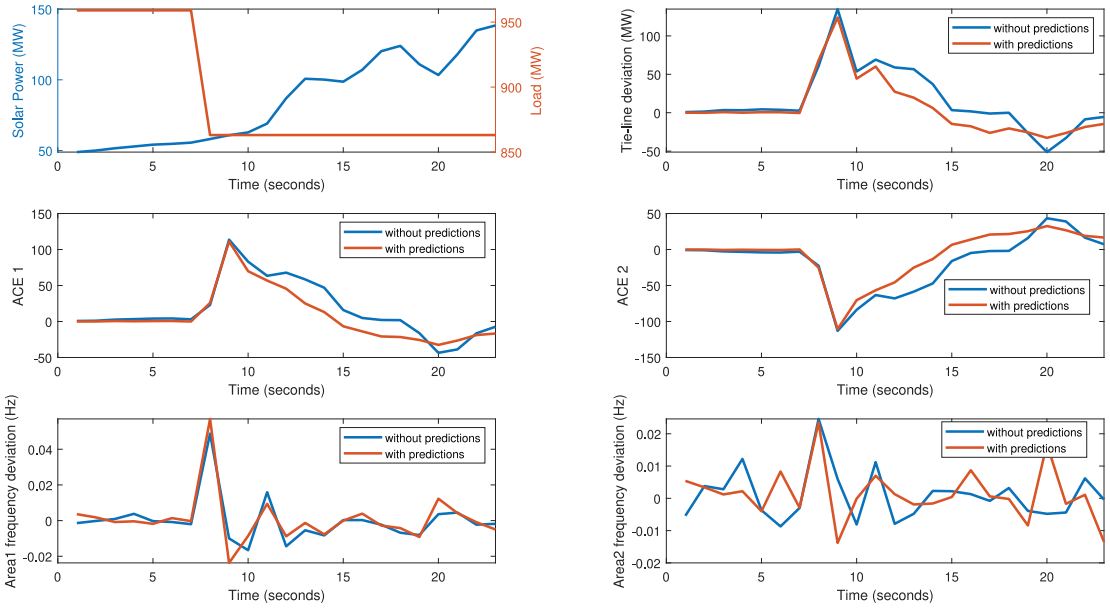

Fig. 11. (a) PV power, (b) Tie-line Power deviation, (c)Area-1 ACE, (d) Area-2 ACE, (e) Area-1 frequency deviation, and (f) Area-2 frequency deviation observed when load is reduced by 20% and PV power increased by 50%.

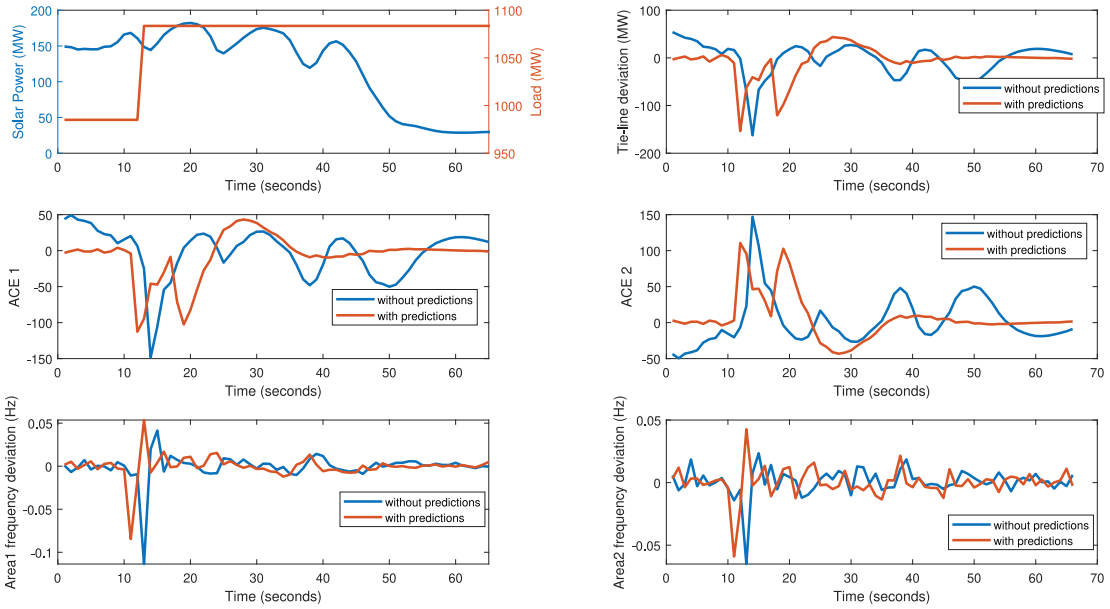

Fig. 12. (a) PV power, (b) Tie-line Power deviation, (c)Area-1 ACE, (d) Area-2 ACE, (e) Area-1 frequency deviation, and (f) Area-2 frequency deviation observed when load is increased by 20% and PV power decreased by 50%.

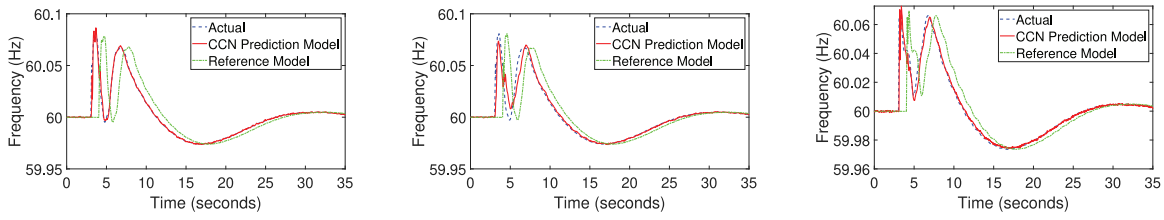

(a) Bus 6 (b) Bus 7 (c) Bus 8

Fig. 13. Actual, CCN predicted, and reference model frequencies when PMU at Bus 7 is under attack.

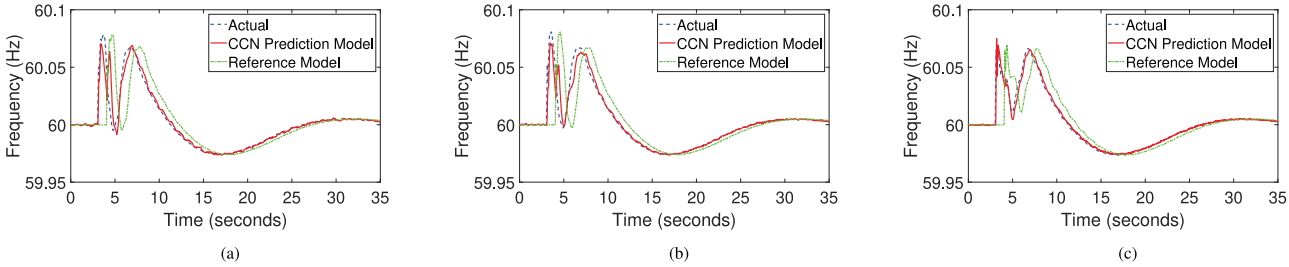

Fig. 14. Actual, CCN predicted, and reference model frequencies when PMUs at Bus 7 and Bus 6 are under attack.

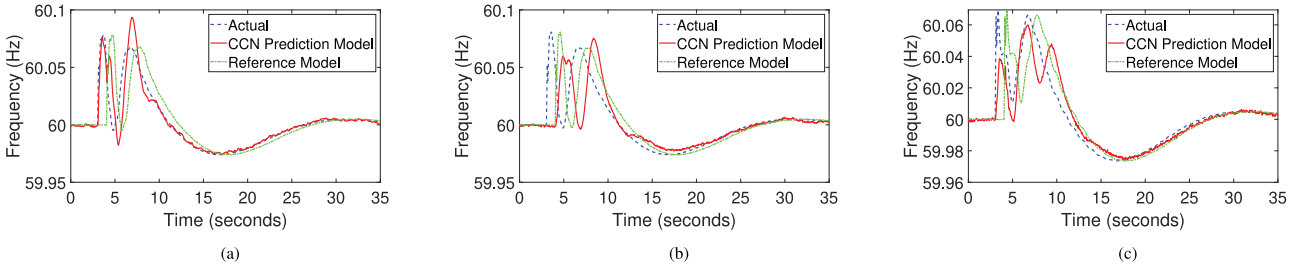

Fig. 15. Actual, CCN predicted, and reference model frequencies when PMUs at Bus 7, Bus 6, and Bus 8 are under attack.

TABLE V
CCESN BASED FREQUENCY PREDICTION PERFORMANCE UNDER DOS ATTACK

Accuracy Measure	Bus 7 is Attacked			Bus7 and Bus 6 are Attacked			Bus7, Bus 6, and Bus 8 are Attacked		
	Bus7	Bus 6	Bus 8	Bus7	Bus 6	Bus 8	Bus7	Bus 6	Bus 8
$SF(\%)$	85	97	94	84	84	94	68	-10	51
$MAPE(\%)$	1.30×10^{-03}	7.37×10^{-04}	9.68×10^{-04}	1.5×10^{-03}	1.28×10^{-03}	9.03×10^{-04}	2.57×10^{-03}	5.29×10^{-03}	2.94×10^{-03}

TABLE VI
PERFORMANCE COMPARISON UNDER DOS ATTACK

Metric		Scenario 2 Blocked PMU 7	Countermeasure A Blocked PMU 7	Countermeasure B Blocked PMU 7	Countermeasure C		
					Blocked PMU 7	Blocked PMUs 6 and 7	Blocked PMUs 6, 7 and 8
CF_{1min} count	Positive	29	37	37	26	30	29
	Negative	32	24	24	35	32	34
Accumulated CF_{1min}		6.67	0.6866×10^{-7}	0.1043×10^{-6}	0.1008×10^{-6}	0.1030×10^{-6}	0.1043×10^{-6}
$CPS1(\%)$		-5.8458e+06	199.9399	199.9086	199.9117	199.9097	199.9086
$CPS2_{10min}(\%)$		100	100	100	100	100	100
$CPS2_{4s}(\%)$		0.64	91	91	95	94	94
$total-violated_{ACE_{4s}}$		918	79	83	47	50	46
$CPS2_{1s}(\%)$		0.67	91	92	95	95	95
$total-violated_{ACE_{1s}}$		3674	313	297	170	172	175

However, the AGC performance is dropped with the increasing number of PMUs are under attack. This is due to the degrading accuracy of the VSN predictions.

V. CONCLUSION

In this paper, an enhanced tie-line bias control method is proposed for a power system in uncertain environments. Tie-line bias control is performed using an automatic generation control with the introduction of PV power and bus frequency predictions. Predictions are introduced to overcome the response time of the AGC and governors of the system. PV power predictions are obtained using an echo state network and bus frequency predictions are obtained using a virtual synchrophasor network (VSN). The VSN is based on cellular computational echo state network. The cells of CCESN, virtual PMUs, provides resiliency to physical PMUs. It is shown that the prediction models provide better accuracies in predicting PV power and

bus frequencies compared to state-of-art persistence model. Application of the prediction models in AGC operation provides enhanced tie-line bias control for different weather and load conditions. Furthermore, the VSN is capable of mitigating impact(s) of denial of service attacks on physical PMUs. The tie-line bias control performance is measured using NERC defined standard performance metrics ($CPS1$ and $CPS2$) and related metrics, which indicate this method can minimize the penalties introduced by NERC for maintaining steady state interconnection frequency. Future work includes analyzing DoS attacks on both physical and virtual PMUs and developing mitigation strategies.

APPENDIX A

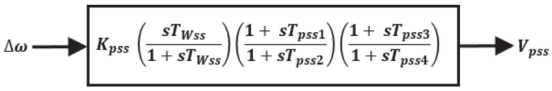

Fig. A.16. Power System Stabilizer (PSS).

TABLE A.7
AGC PARAMETERS

	λ_R	T (s)	k	α_1	α_2
AGC-1	-20	0.5	0.007	0.5	0.5
AGC-2	-20	0.5	0.007	0.5	0.5

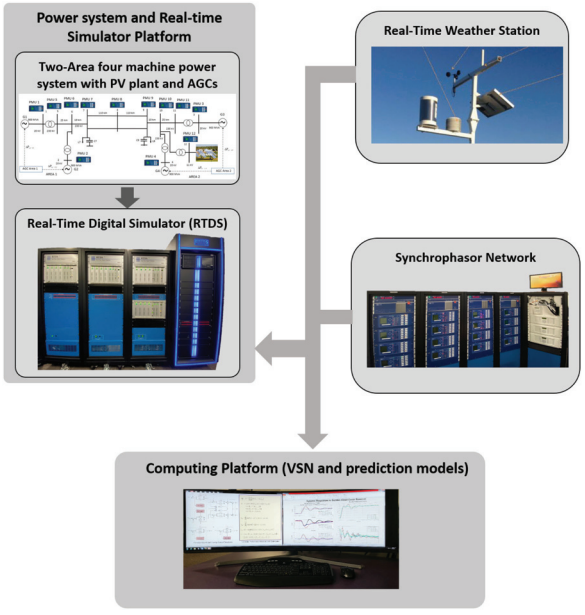

Fig. A.17. Experimental setup for tie-line bias control study.

REFERENCES

[1] Solar industry research data. Solar Energy Industries Association: SEIA. Accessed: Jun. 25, 2020. [Online]. Available: https://www.seia.org/solar-industry-research-data

[2] N. A. E. R. C. (NERC), "Balancing and frequency control," 2011.

[3] H. Bevrani and T. Hiyama, *Intelligent Automatic Generation Control*. Boca Raton, Florida: CRC Press, 2017.

[4] National Renewable Energy Laboratory (NREL), *Grid-friendly renewable energy: Solar and wind participation in automatic generation control systems*. Accessed: Jun. 25, 2020. [Online]. Available: https://www.nrel.gov/docs/fy19osti/73866.pdf

[5] X. Zhang, Z. Xu, T. Yu, B. Yang, and H. Wang, "Optimal mileage based AGC dispatch of a genco," *IEEE Trans. Power Systems*, vol. 35, no. 4, pp. 2516–2526, Jul. 2020.

[6] L. Yin, S. Li, and H. Liu, "Lazy reinforcement learning for real-time generation control of parallel cyberphysicalsocial energy systems," *Eng. Appl. Artif. Intell.*, vol. 88, 2020, Art. no. 103380.

[7] X. Zhao, Z. Lin, B. Fu, L. He, and C. Li, "Research on the predictive optimal pid plus second order derivative method for agc of power system with high penetration of photovoltaic and wind power," *J. Elect. Eng. Technol.*, vol. 14, p. 1075–1086, 2019.

[8] H. Luo, Z. Hu, H. Zhang, and H. Chen, "Coordinated active power control strategy for deloaded wind turbines to improve regulation performance in agc," *IEEE Trans. Power Syst.*, vol. 34, no. 1, pp. 98–108, Jan. 2019.

[9] Y. Wei, I. Jayawardene, and G. K. Venayagamoorthy, "Optimal automatic generation controllers in a multi-area interconnected power system with utility-scale PV plants," *IET Smart Grid*, vol. 2, no. 4, pp. 581–593, 2019.

[10] X. Zhong, I. Jayawardene, G. K. Venayagamoorthy, and R. Brooks, "Denial of Service Attack on Tie-Line Bias Control in a Power System With PV Plant," *IEEE Trans. Emerg. Top. Comput. Intell.*, vol. 1, no. 5, pp. 375–390, Oct. 2017.

[11] S. Alhalali, C. Nielsen, and R. El-Shatshat, "Mitigation of cyber-physical attacks in multi-area automatic generation control," *Int. J. Elect. Power Energy Syst.*, vol. 112, pp. 362–369, 2019.

[12] R. K. Mishra and K. S. Swarup, "Adaptive weight-based self reconfiguration of smart distribution network with intelligent agents," *IEEE Trans. Emerg. Top. Comput. Intell.*, vol. 2, no. 6, pp. 464–472, Dec. 2018.

[13] I. Jayawardene, R. V. Kulkarni, and G. K. Venayagamoorthy, "CI-based analytics for photovoltaic power predictions and tie-line bias control in smart grid," in *Proc. IEEE Symp. Ser. Comput. Intell.*, 2018, pp. 1626–1633.

[14] P. Gotseff, J. Cale, M. Baggu, D. Narang, and K. Carroll, "Accurate power prediction of spatially distributed PV systems using localized irradiance measurements," in *Proc. IEEE PES Gen. Meeting Conf. Expo.*, Jul. 2014, pp. 1–5.

[15] C. Lynch, M. J. O'Mahony, and R. A. Guinee, "A novel 24 kalman filter bank estimator for solar irradiance prediction for PV power generation," in *Proc. IEEE 42nd Photovolt. Specialist Conf.*, Jun. 2015, pp. 1–7.

[16] J. Rodway, P. Musilek, S. Misak, and L. Prokop, "Prediction of PV power quality: Total harmonic distortion of current," in *Proc. IEEE Elect. Power Energy Conf.*, Aug. 2013, pp. 1–4.

[17] J. Dong, X. Ma, S. M. Djouadi, H. Li, and T. Kuruganti, "Real-time prediction of power system frequency in fnet: A state space approach," in *Proc. IEEE Int. Conf. Smart Grid Commun.*, Oct 2013, pp. 109–114.

[18] Q. Bo, X. Wang, and K. Liu, "Minimum frequency prediction of power system after disturbance based on the v-support vector regression," in *Proc. Int. Conf. Power Syst. Technol.*, Oct. 2014, pp. 614–619.

[19] R. Arablouei, S. Werner, and K. Dogancay, "Estimating frequency of three-phase power systems via widely-linear modeling and total least- squares," in *Proc. 5th IEEE Int. Workshop Computat. Adv. Multi-Sensor Adaptive Process.*, Dec. 2013, pp. 464–467.

[20] H. Jaeger, "The "echo state" approach to analysing and training recurrent neural networks," *National Research Center for Information Technology*, GMD Report, Tech. Rep., vol. 148, p. 13, 2001.

[21] C. Gallicchio, A. Micheli, and L. Pedrelli, "Comparison between Deep-ESNs and gated RNNs on multivariate time-series prediction," *CoRR*, vol. abs/1812.11527, Dec. 2018. [Online]. Available: http://arxiv.org/abs/1812.11527

[22] B. Luitel and G. K. Venayagamoorthy, "Cellular computational networksa scalable architecture for learning the dynamics of large networked systems," *Neural Networks*, vol. 50, pp. 120–123, 2014. [Online]. Available: http://www.sciencedirect.com/science/article/pii/S0893608013002529

[23] B. Luitel and G. K. Venayagamoorthy, "Decentralized asynchronous learning in cellular neural networks," *IEEE Trans. Neural Netw. Learn. Syst.*, vol. 23, no. 11, pp. 1755–1766, Nov. 2012.

[24] P. Arunagirinathan, H. A. Abdelsalam, and G. K. Venayagamoorthy, "Remote power system stabilizer tuning using synchrophasor data," in *Proc. IEEE Symp. Comput. Intell. Appl. Smart Grid.*, 2014, pp. 1–7.

[25] A. Arzani and G. K. Venayagamoorthy, "Computational approach to enhance performance of photovoltaic system inverters interfaced to utility grids," *IET Renewable Power Gener.*, vol. 12, no. 1, pp. 112–124, 2018.

[26] I. Jayawardene and G. K. Venayagamoorthy, "Reservoir based learning network for control of two-area power system with variable renewable generation," *Neurocomputing*, vol. 170, pp. 428–438, 2015.
[27] G. K. Venayagamoorthy and B. Shishir, "Effects of spectral radius and settling time in the performance of echo state networks," *Neural Networks*, vol. 22, no. 7, pp. 861–863, 2009. [Online]. Available: http://www.sciencedirect.com/science/article/pii/S0893608009000665
[28] M. Lukoševičius, "A practical guide to applying echo state networks," in *Neural Networks: Tricks Trade*. Berlin, Germany: Springer, 2012, pp. 659–686.
[29] C. F. Coimbra and H. T. Pedro, "Chapter 15 - Stochastic-Learning Methods," in *Solar Energy Forecasting Resour. Assessment*, J. Kleissl, Ed. Boston: Academic Press, 2013, pp. 383–406.
[30] *IEEE standard for synchrophasor data transfer for power systems IEEE* Standard C37.118.2-2011, pp. 1–53, 2011.

Iroshani Jayawardene (Student Member, IEEE) received the B.Sc. degree (Hons.) in computer science from the University of Peradeniya, Sri Lanka, in 2011. She received the Ph.D. degree in computer engineering from the Clemson University, Clemson, SC, USA, in December 2020. After working as a Software Engineer for three years, she joined the Real-Time Power and Intelligent Systems Laboratory as a Research Assistant. She was a Collaborative Researcher with NREL from October 2019 to March 2020. Her current research interests include smart grid, real-time power system data analytics, and artificial intelligence. She was nominated as a finalist for Best Student Paper Award competition at IEEE 43rd PVSC, 2016. She was the recipient of the INNS Conference on Big Data student travel grant in 2015 and IEEE SSCI student travel grant in 2017.

Ganesh Kumar Venayagamoorthy (Fellow, IEEE) received the B.Eng. (Hons.) degree from Abubakar Tafawa Balewa University, Bauchi, Nigeria, in March 1994. He holds the M.B.A. degree in entrepreneurship and innovation from Clemson University, SC, in 2016. He received the M.Sc.Eng. and Ph.D. degrees in electrical engineering from the University of Natal, Durban, South Africa, in April 1999 and February 2002, respectively. He is the Duke Energy Distinguished Professor with Power Engineering and Professor with Electrical and Computer Engineering and Automotive Engineering, Clemson University. Prior to that, he was a Professor with Electrical and Computer Engineering, the Missouri University of Science and Technology (Missouri ST), Rolla, USA, from 2002 to 2011 and Senior Lecturer with the Department of Electronic Engineering, Durban University of Technology, Durban, South Africa, from 1996 to 2002. In 2004, he was the Founder and Director of the Real-Time Power and Intelligent Systems Laboratory. He holds an Honorary Professor position with the School of Engineering, the University of Kwazulu-Natal, Durban, South Africa. He has authored or coauthored more than 500 refereed technical articles. His publications are cited 19,000 times with a h-index of 65 and i10-index of 270. His research interests focuses on development and innovation of smart grid technologies and operations. He is an inventor of technologies for scalable computational intelligence for complex systems and dynamic stochastic optimal power flow. He led the brain2grid project funded by US NSF. He has given over 500 invited keynotes, plenaries, presentations, tutorials and lectures in over 40 countries to date. He is involved in the leadership and organization of many conferences including the General Chair of the Power System Conference (Clemson, SC, USA) since 2013, and Pioneer and Chair/Co-Chair of the IEEE Symposium of Computational Intelligence Applications in Smart Grid (CIASG) since 2011. He is currently the Chair of the IEEE PES WORKING GROUP ON INTELLIGENT CONTROL SYSTEMS, and the Founder and Chair of IEEE Computational Intelligence Society (CIS) Task Force on Smart Grid. He has served/serves as Editor/Guest Editor for several IEEE TRANSACTIONS AND ELSEVIER JOURNALS. He is a fellow of the IET (U.K.) and the SAIEE.

Xingsi Zhong received the B.S. degree in math from Jilin University, Changchun, China, in 2010 and the M.S. degree in computer science from the University of Texas Pan-American, Edinburg, TX, USA, in 2013. He received the Ph.D. degree from the Holcombe Department of Electrical and Computer Engineering, Clemson University, Clemson, SC, USA. He is currently a Senior Staff Engineer in Palo Alto Networks Inc., Sunnyvale, CA, USA. His research interests include scalability, time-series analysis, sidechannel analysis, cyber-physical system security, and computational intelligence.